# Compression forces generated by actin comet tails on lipid vesicles

**Paula A. Giardini, Daniel A. Fletcher*, and Julie A. Theriot†**

Department of Biochemistry, Stanford University School of Medicine, Stanford, CA 94305-5307

Communicated by James A. Spudich, Stanford University School of Medicine, Stanford, CA, March 21, 2003 (received for review September 4, 2002)

**Polymerizing networks of actin filaments generate force for a variety of movements in living cells, including protrusion of filopodia and lamellipodia, intra- and intercellular motility of certain bacterial and viral pathogens, and motility of endocytic vesicles and other membrane-bound organelles. During actin-based motility, coexisting populations of actin filaments exert both pushing and retarding forces on the moving cargo. To examine the distribution and magnitude of forces generated by actin, we have developed a model system where large artificial lipid vesicles coated with the protein ActA from the bacterial pathogen *Listeria monocytogenes* are propelled by actin polymerization in cytoplasmic extract. We find that motile vesicles associated with actin comet tails are significantly deformed due to an inward compression force exerted by actin polymerization orthogonal to the direction of motion, which is >10-fold greater in magnitude than the component of the force exerted in the direction of motion. Furthermore, there is a spatial segregation of the pushing and retarding forces, such that pushing predominates along the sides of the vesicle, although retarding forces predominate at the rear. We estimate that the total net (pushing minus retarding) force generated by the actin comet tail is ≈0.4–4 nN. In addition, actin comet tail formation is associated with polarization of the ActA protein on the fluid vesicle surface, which may reinforce the persistence of unidirectional motion by helping to maintain a persistent asymmetry of actin filament density.**

Force generation is fundamental to many biological processes, such as muscle contraction, organelle transport, and cellular motility. Cells use a variety of mechanisms to store and transduce chemical energy to produce useful mechanical work. For example, the molecular motor proteins myosin and kinesin generate forces through conformational changes coupled to ATP hydrolysis, allowing these proteins to walk along actin or microtubule tracks in a stepwise manner. The force generated by such motor proteins has been precisely measured and extensively studied (1, 2). Polymerizing protein filaments such as actin and microtubules can also convert chemical energy into mechanical force, requiring only a nonequilibrium polymerization reaction to transduce chemical free energy to useful mechanical work (3, 4). However, the magnitude and mechanism of force generation by protein polymerization are poorly understood compared with classical motor proteins, despite a broad range of biological processes that use this method of force generation (5–13).

Pathogenic bacteria, viruses, and endocytic vesicles that use actin polymerization-based mechanisms for motility are associated with a characteristic actin "comet tail" structure (7) formed from a large number of actin filaments crosslinked in a dendritic meshwork (14). New actin filaments are continuously nucleated at the cargo surface by using any of a variety of biochemical mechanisms, resulting in the local activation of the Arp2/3 complex, which catalyzes actin filament nucleation and filament branch formation (15). The Gram-positive bacterial pathogen *Listeria monocytogenes*, for example, initiates local actin polymerization in an infected host cell by using a surface-bound virulence protein, ActA (16), which directly activates Arp2/3 (17, 18), whereas endocytic vesicles use more complex and indirect mechanisms for Arp2/3 activation (10, 12, 19). Localization of any of several different Arp2/3-activating factors to an organelle-sized object can generate formation of comet tails with similar overall structures that propel objects at comparable speeds, suggesting that it is the force exerted by the organized polymerizing meshwork of actin filaments and not the specific identity of the surface nucleation factor that results in movement.

Recently, the development of increasingly simplified reconstituted motility systems where bacteria or artificial cargos are propelled by actin comet tails (20–23) has made it possible to perturb and study the biochemical and biophysical parameters governing polymerization-based motility. In addition, several detailed biophysical models (24–28) have been formulated to predict the magnitude and direction of the forces generated by actin polymerization in the comet tail. Here we describe a membrane-based reconstituted motility system that has enabled us to measure the spatial distribution and approximate magnitude of the forces generated by actin in a motile comet tail. Our results are in agreement with the major qualitative predictions of a class of mesoscopic biophysical models that consider elastic energy stored in the growing comet tail actin gel as a major modality of force transduction, but they disprove several quantitative predictions of published versions of these models (23, 26, 29, 30). Furthermore, our results extend the predictions of a microscopic model where coexisting populations of actin filaments can exert both retarding and pushing forces (27, 31).

## Materials and Methods

Large multilamellar vesicles were prepared from a 46:50:2:2 molar ratio of phosphatidylcholine/cholesterol/fluorescein-phosphatidylethanolamine/Ni-NTA chelating lipid. Further details of vesicle preparation and coating of polystyrene beads with lipid monolayers can be found in *Supporting Text*, which is published as supporting information on the PNAS web site, www.pnas.org. His-tagged ActA was purified as previously described (18, 21) and adsorbed on the surface of vesicles and lipid-coated beads at saturating amounts (≈$10^7$ molecules per bead estimated by quantitative Western blot). Motility assays were adapted from ref. 21. ActA-coated vesicles were added to *Xenopus laevis* egg cytoplasmic extract diluted to 40% of original protein concentration with *Xenopus* extract buffer (32) doped with tetramethylrhodamine iodoacetamide-labeled monomeric actin and ATP regenerating mix (32). Vesicle motility was visualized on a Zeiss Axioplan microscope equipped with phase contrast and epifluorescence optics by using a ×63, numerical aperture 1.4 objective and a back-thinned cooled charge-coupled device camera (Princeton Instruments, Trenton, NJ). Phase-contrast, fluorescein, and rhodamine images were acquired every 5 s. Quantitative measurements and data analysis were performed by using METAMORPH software (Universal Imaging, Media, PA). See *Supporting Text* for further details of data analysis.

*Present address: Department of Bioengineering, University of California, Berkeley, CA 94720.

†To whom correspondence should be addressed. E-mail: theriot@stanford.edu.

## Results

**Observation of Vesicle Deformation by Actin Polymerization.** We have developed a model system where artificial lipid vesicles ranging in size from a few hundred nanometers to tens of micrometers are propelled by actin comet tails nucleated by a form of the *L. monocytogenes* ActA protein (21) (see Movies 1–3, which are published as supporting information on the PNAS web site). Most vesicles associated with comet tails were ≈1–5 $\mu$m in diameter, although occasionally much larger membranous structures of varying shapes also nucleated actin and moved unidirectionally (Movie 2). Some actin-associated vesicles could be observed budding from larger membrane masses. During budding, actin filaments accumulated in a collar around the neck of the nascent vesicle. Further polymerization caused the neck to stretch, eventually forming a persistent lipid tubule tether running down the core of the comet tail (Movie 3). These tethers would occasionally snap, liberating a motile actin-associated vesicle that often resorbed the trailing lipid tubule (Movie 1).

Free motile ActA-coated vesicles associated with actin comet tails were deformed, exhibiting an asymmetrical tear-drop shape with the longer axis parallel to the direction of motion and the end with highest curvature associated with the comet tail. In contrast, similarly prepared control vesicles not coated with ActA (and therefore not associated with actin) usually adopted a symmetrical spherical or prolate spheroid shape in cytoplasmic extract (Fig. 1 *A* and *B*). To determine whether this qualitative shape difference was significant, we measured the major and minor axes on images of 121 ActA-coated, actin-associated vesicles and 242 control vesicles of similar sizes. Ninety-eight percent of actin-associated vesicles were tear-drop shaped, compared with only 7% of control vesicles. (Fig. 1 *C* and *D*). Similar distorted shapes have been reported for native endocytic vesicles associated with actin comet tails (12).

The characteristic distorted shape suggested that the comet tails exerted an inward compression force, orthogonal to the direction of motion, that pinched the rear of the vesicles. Consistent with this idea, we observed that the total volume of most vesicles decreased slowly over time, presumably as water was squeezed out through the semipermeable lipid bilayer (average volume loss 0.006 $\mu m^3$/s, or ≈0.0004 volume/s). The observation of compression forces generated by actin comet tails is consistent with a class of biophysical models that focus on accumulation of stress in the crosslinked actin gel as a major modality of force storage and transduction (23, 26, 29, 30) but has not previously been demonstrated experimentally.

**Actin-Dependent Polarization of ActA Protein.** It was initially surprising that such large vesicles (≈5 $\mu$m in diameter) were able to form actin comet tails, because under similar conditions polystyrene beads coated with immobilized ActA cannot break symmetry to form a polarized comet tail if their diameter is >2 $\mu$m (21). However, large beads coated asymmetrically with ActA can form polarized comet tails (21). We therefore hypothesized that lateral movement of ActA on the surface of the fluid phospholipid bilayer might facilitate symmetry-breaking for vesicles. We compared the distribution of fluorescently labeled ActA (Fig. 2*B*, blue curve) on vesicles associated with actin comet tails with fluorescently labeled lipid (Fig. 2*A*, green curve) in similar vesicles and found a striking specific accumulation of ActA at the rear of the vesicle (Fig. 2 *A* and *B*; Movie 4, which is published as supporting information on the PNAS web site). The distribution of ActA closely paralleled the distribution of actin filaments (Fig. 2*B*, red curve). Although ActA has not been shown to bind directly to actin filaments, ActA is known to bind F-actin indirectly via VASP and the Arp2/3 complex (33–35), so it seems likely that the polarization of ActA on motile

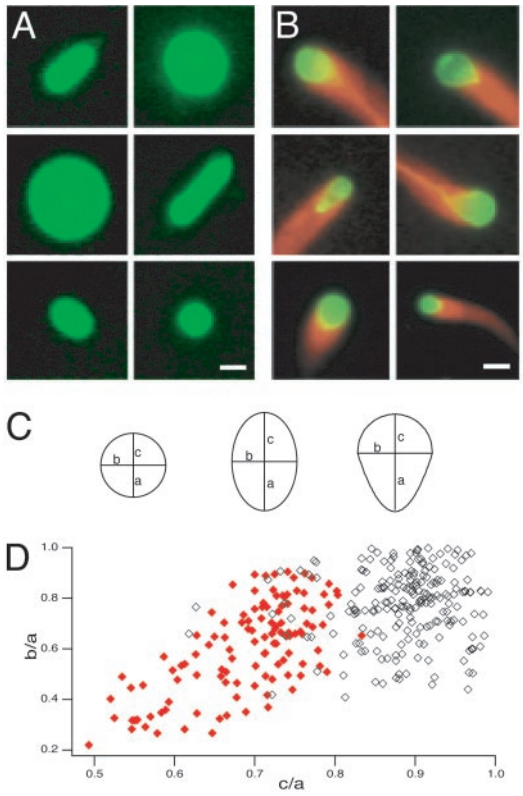


**Fig. 1.** Actin-based deformation of large ActA-coated lipid vesicles in cytoplasmic extracts. (*A*) Shapes of control vesicles in *Xenopus* egg cytoplasmic extract. Pseudocolored images show typical spherical and prolate spheroid vesicle shapes. Green, fluorescein-phosphatidylethanolamine. (Bar = 3 $\mu$m.) (*B*) Shapes of ActA-coated vesicles with actin comet tails in *Xenopus* egg cytoplasmic extract. Pseudocolor images show sample frames from six time-lapse movies of vesicles associated with comet tails. Red, rhodamine-actin; green, fluorescein-phosphatidylethanolamine. The regions of overlap between red and green signals appear yellow. Vesicles associated with actin are asymmetrically deformed to a tear-drop shape. (Bar = 3 $\mu$m.) See *Supporting Text* for details on pharmacological manipulations of motility assays. (*C*) Definitions for measured parameters for circular, elliptical, and tear-drop vesicle profiles. For a perfect circle, a = b = c. For a perfect ellipse, a = c > b. For a tear-drop, a > b and a > c. (*D*) Scatter plot of shape distribution for ActA-coated (red, closed diamonds) and control (black, open diamonds) vesicles in *Xenopus* extract. The longest semiaxis is defined as a, so b/a and c/a can assume values ≤1. Control vesicles were usually nearly circular (where b/a and c/a >0.8; $n$ = 127/241) or elliptical (where b/a <0.8 and c/a >0.8; $n$ = 96/241). Nearly all moving ActA-coated vesicles associated with comet tails were tear-drop shaped (where c/a <0.8; $n$ = 118/121). Both b/a and c/a were significantly smaller for the population of actin-associated vesicles than for the population of control vesicles ($P < 0.0001$ by Student's $t$ test), indicating that the actin comet tails caused the vesicles to become both narrower and more asymmetrical.

vesicles was due to its indirect binding to actin filaments in the comet tail.

To determine whether this ActA asymmetry was due solely to actin-based forces acting on a fluid membrane surface or whether variations in membrane curvature might also affect ActA distribution, we examined the distribution of ActA on the surface of large (1.5-$\mu$m-diameter) hydrophobic polystyrene beads coated with a lipid monolayer in association with actin comet tails. The surface of these beads is approximately as fluid as a simple lipid bilayer (36), but the beads are not deformable. We found substantial accumulation of ActA on the rear half of the bead, suggesting that the actin-dependent ActA polarization could occur independently of deformation (Fig. 2 *C* and *D*). Because ActA catalyzes nucleation of new actin filaments via its

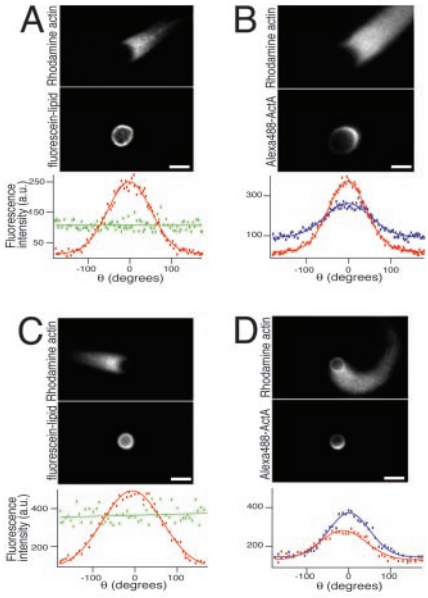


**Fig. 2.** Polarized ActA distribution on motile vesicles. (*A*) Control distribution of fluorescein-phosphatidylethanolamine on a large actin-associated ActA-coated lipid vesicle. (*Top*) Rhodamine-actin fluorescence showing comet tail. (*Middle*) Lipid distribution. (*Bottom*) Fluorescence intensity of actin (red) and fluorescent lipid (green) around the vesicle, plotted as a function of angular position ($\theta$, defined where $\theta = 0$ at the pointed end of the vesicle; see Fig. 3*B*). (Bars = 2 $\mu$m.) (*B*) Asymmetric distribution of ActA. (*Top*) Rhodamine-actin fluorescence showing comet tail. (*Middle*) Distribution of fluorescently labeled ActA. (*Bottom*) Fluorescence intensity of actin (red) and fluorescent ActA (blue) around the vesicle, plotted as a function of angular position ($\theta$). Both ActA and actin are asymmetrically distributed with the peak intensity at $\theta = 0$. This is a wide-field image and therefore does not quantitatively reflect the ActA and actin densities (see Movie 4). (*C*) Control distribution of fluorescein-phosphatidylethanolamine in a monolayer on an actin-associated polystyrene bead coated with ActA. (*Top*) Rhodamine-actin fluorescence showing comet tail. (*Middle*) Lipid distribution. (*Bottom*) Fluorescence intensity of actin (red) and fluorescent lipid (green) around the bead, plotted as a function of angular position ($\theta$). (*D*) Asymmetric distribution of ActA on an actin-associated polystyrene bead coated with a phospholipid monolayer. (*Top*) Rhodamine-actin fluorescence showing comet tail. (*Middle*) Distribution of fluorescently labeled ActA. (*Bottom*) Fluorescence intensity of actin (red) and fluorescent ActA (blue) around the bead. Both ActA and actin are asymmetrically distributed. The slight shift between the peak of the ActA distribution and the peak of the actin distribution is due to the curvature of this comet tail.

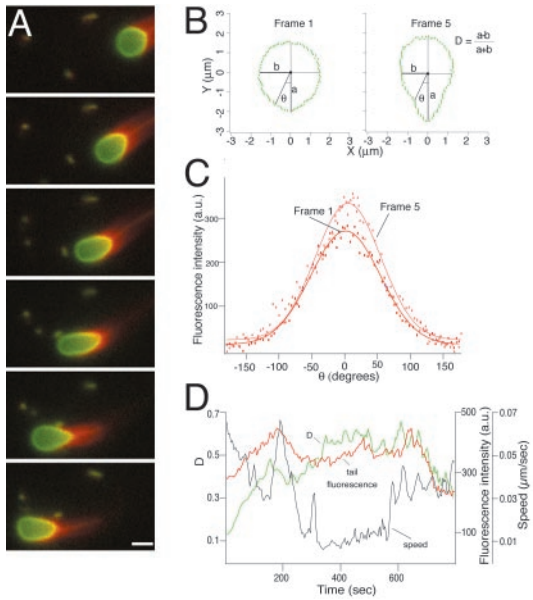


**Fig. 3.** Motion analysis of ActA-coated lipid vesicles in cytoplasmic extracts. (*A*) Sequence of six frames from a time-lapse movie, separated by 35-s intervals, showing actin-dependent movement and deformation of an ActA-coated lipid vesicle in *Xenopus* egg cytoplasmic extract. Red, rhodamine-actin; green, fluorescein-phosphatidylethanolamine. The regions of overlap between red and green signals appear yellow. As the vesicle moves from right to left, it becomes increasingly elongated in frames 1–4 and then less elongated in frames 5 and 6. (Bar = 2 $\mu$m.) See Movie 1. (*B*) Outlines of the vesicle shown in *A* at frame 1 (nearly spherical) and frame 5 (elongated), reoriented so that the longest axis is vertical. The degree of deformation was measured for each frame as the dimensionless quantity *D*, where $D = (a - b)/(a + b)$. $D = 0$ for a perfect circle, and $D = 1$ for a straight line. At frame 1, $D = 0.11$, and at frame 5, $D = 0.38$. (*C*) Angular distribution of actin filament density around the vesicle shown in *A* for frames 1 (red) and 5 (pink). $\theta = 0$ at the back (pointed end) of the vesicle. Rhodamine-actin fluorescence intensity (arbitrary units) was measured for each pixel for the outlines shown in *B* and plotted as a function of angular position around the vesicle. Thin lines are best-fit Gaussian curves. Although the exact shape of the actin filament density distribution varies slightly from frame to frame, the peak density is always found near $\theta = 0$ and generally falls to half-peak at about $\theta = \pm 50°$. (*D*) Changes over time in vesicle speed (black), deformation (green), and peak actin density (red) for the vesicle shown in *A*. See *Supporting Text* for details on quantitative image analysis.

interaction with Arp2/3 (18), it is likely that actin-dependent ActA polarization in turn contributes to maintaining a persistent asymmetry of actin filament density on the vesicle surface and thus reinforcing persistent unidirectional motion over time.

**Analysis of Vesicle Motion.** To understand how vesicle shape changes correlated with changes in speed and actin tail dynamics, we recorded and analyzed phase-contrast and fluorescent time-lapse movies of a large number of untethered moving vesicles (Fig. 3*A*; Movie 1, for example). Individual vesicles underwent significant changes in degree of deformation, speed, and comet tail actin density over periods of several minutes (Fig. 3).

Our data set included movies of 121 actin-associated vesicles. The mean vesicle size in the measured population was 2.9 $\mu$m in equivalent spherical diameter (SD; SD = 1.0 $\mu$m). These vesicles underwent a broad range of deformation, where the mean D was 0.29 (SD = 0.16; Fig. 4*A*). Speeds also varied throughout the population as well as over the course of each movie (mean = 0.05 $\mu$m/s, SD = 0.04; Fig. 4*B*). There were no correlations between the degree of vesicle deformation and speed, size, or tail fluorescence over the population as a whole (Fig. 4 *C* and *D*).

Variability in membrane tension among the vesicles in the population might mask informative correlations between vesicle deformation and speed or actin density. Therefore, we examined the correlations between time-dependent changes in those three parameters for each individual vesicle. For all tracks longer than 200 s ($n = 39$), we calculated the cross-correlation coefficient between deformation and speed ($R_{ds}$), deformation and peak fluorescence intensity ($R_{df}$), and speed and peak fluorescence intensity ($R_{sf}$). Across the population, the mean values of $R_{ds}$ and $R_{df}$ were not significantly different from zero (0.07 and $-0.03$). The mean value of $R_{sf}$ was $-0.39$, which is statistically significant at $P < 0.01$ by Student's *t* test. In other words, during segments of each movie where the peak actin comet tail density was higher than average, speed was likely to be lower than average (Fig. 4*E*; see *Supporting Text*). Thus, changes in vesicle speed appeared to be coupled to changes in the comet tail actin filament density, such that comet tails became more dense as their associated vesicles slowed down. However, the forces responsible for vesicle deformation appeared to be largely independent of the forces responsible for determining net vesicle speed.

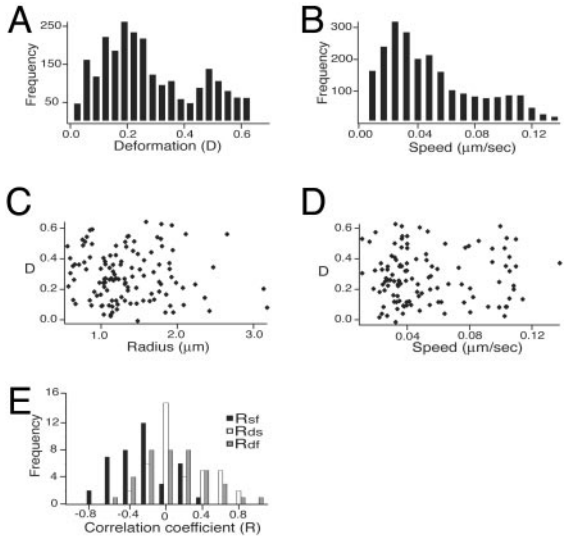


**Fig. 4.** Distribution of deformation, speed, and size across a population of motile vesicles. (*A*) Distribution of instantaneous deformations. Deformation was measured for each video frame (separated at 5-s intervals) for 121 vesicles. The mean measured deformation for this population was 0.29 ± 0.16. (*B*) Distribution of speeds. Speed was measured for the interval between each adjacent pair of video images. Most vesicles exhibited large changes in speed over the course of each time-lapse movie. The mean speed was 0.05 ± 0.04 $\mu$m/s. (*C*) Scatterplot of vesicle deformation and size. There is no correlation between the average D for each individual vesicle and its size ($R$ = average unstressed spherical radius in micrometers). (*D*) Scatterplot of vesicle deformation and speed. There is no correlation between the average D for each individual vesicle and its average speed. (*E*) Distribution of intratrack crosscorrelation coefficients. Crosscorrelation coefficients for deformation and speed ($R_{ds}$, white bars) and deformation and tail fluorescence ($R_{df}$, gray bars) are symmetric around zero (mean values 0.07 and −0.03, respectively). In contrast, crosscorrelation coefficients for speed and tail fluorescence ($R_{sf}$, black bars) are mostly negative (mean = −0.39). See *Supporting Text* for further details on statistical analysis of individual vesicle behavior.

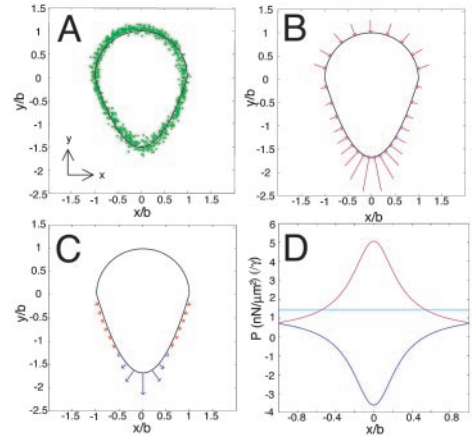


**Fig. 5.** Quasistatic model for actin-dependent forces at the surface of deformed vesicles. (*A*) Outlines of vesicles near the mean size (equivalent spherical radius = 1.41−1.48 $\mu$m) and mean deformation (D = 0.25–0.29) were measured and normalized to derive an average exact vesicle shape. Green circles show all individual pixel positions. The front half of the averaged vesicle (top) is well fit by a semicircle (black line); thus for the average vesicle $b = c$ (see Fig. 1*C*). The rear half (bottom) is well fit by a parabola (black line) (it is also reasonably well fit by a semiellipse). (*B*) Pressure due to membrane tension. Pressure varies with local membrane curvature. Graphical representation of the direction and relative magnitude of inward pressure due to membrane tension for the canonical vesicle shape derived in *A*, shown as magenta arrows. (*C*) Calculated net (pushing minus retarding) actin pressure distribution required to generate the canonical vesicle shape. Graphical representation of the direction and magnitude of normal forces. Places on vesicle surface where pushing forces exceed retarding forces are shown in red; places where retarding forces exceed pushing forces are shown in blue. (*D*) Pressure distributions around the vesicle for $P_\gamma$ (magenta), $P_n$ (blue), and $P_o$ (cyan) in terms of multiples of membrane tension ($\gamma$) on the $y$ axis. Units of mN/m are assumed for $\gamma$.

**Quasistatic Model for Force Distribution.** Next, we wished to determine the spatial distribution of the forces responsible for vesicle deformation. Because the physical properties of artificial phospholipid vesicles have been well characterized (37–42), we were able to use the degree and shape of vesicle deformations as a direct readout of the distribution of the sum of forces acting on the vesicle surfaces. We performed initial calculations on a canonical vesicle shape that represented an average member of the measured population (Fig. 5*A*).

Because our movies showed that each vesicle shape and actin distribution changed only slowly with time, we assumed that the external forces per unit area balanced the internal pressure at every point on the vesicle surface and at every moment in time (i.e., the system is quasistatic). At any given moment in time, the net external pressure applied at each point on the vesicle surface is the sum of pressure due to membrane tension acting inward ($P_\gamma$), and pressure from two coexisting populations of actin filaments within the comet tail: unattached, polymerizing actin filaments pushing normal to the surface ($P_p$) (25), and attached actin filaments exerting a retarding force on the surface ($P_r$) (25, 26, 30). Because the separate effects of these two filament populations are not directly observable in our assay, we calculate only the net (pushing minus retarding) pressure due to actin ($P_n = P_p - P_r$). The internal pressure due to osmotic pressure ($P_o$) is a constant everywhere and exactly balanced by the external pressure in the quasistatic case so that:

$$P_o = P_\gamma + P_n, \qquad [1]$$

where both $P_\gamma$ and $P_n$ can vary with position along the membrane. Hydrodynamic drag is not included in Eq. **1** because the drag associated with movement of a 3-$\mu$m-diameter vesicle through viscous cytoplasm at the observed speeds is <100 fN, according to Stokes' Law (43), and is therefore negligible.

To calculate the distribution of the pressure due to actin, we first determined the distribution and magnitude of the pressure due to membrane tension. The spatial distribution of the pressure $P_\gamma$ due to a constant membrane tension can be readily determined from the vesicle shape alone, because this pressure varies inversely with local membrane surface curvature, such that the pressure due to membrane tension is greatest where the radius of curvature is smallest (Fig. 5*B*). Because the actin filament density on the hemispherical front end of the vesicle was negligible and therefore so was the net actin pressure, the internal osmotic pressure must be

$$P_o = P_\gamma|_{\text{hemisphere}} = \frac{2\gamma}{b}, \qquad [2]$$

where $b$ is the radius of the hemisphere, and $\gamma$ is the membrane tension. On the parabolic rear end of the vesicle, the sum of membrane pressure and actin pressure must balance the osmotic pressure found in Eq. **2**. Thus, the net pressure due to actin can be found from

$$P_n = P_\gamma|_{\text{hemisphere}} - P_\gamma|_{\text{parabola}} = \gamma\left[\frac{2}{b} - \left(\frac{1}{R_1} + \frac{1}{R_2}\right)\right], \qquad [3]$$

where $R_1$ and $R_2$ are the local radii of curvature, and the membrane tension $\gamma$ is assumed to be constant around the vesicle. Eq. **3** shows that net actin pressure scales linearly with

membrane tension and disappears only when $R_1 = R_2 = b$. Net actin pressure required to balance forces due to osmotic pressure and $P_\gamma$ is represented in Fig. 5*C*, and all pressures including membrane pressure around the front and rear of the vesicle are plotted in Fig. 5*D* in terms of multiples of $\gamma$. Actin pressure is positive around the sides, indicating a net pushing force into the vesicle, and negative at the rear, indicating a net retarding force pulling away from the vesicle.

Notably, this analysis suggests that the pressure normal to the vesicle surface that is generated by actin does not scale linearly with actin filament density (see Fig. 3*C*), in contrast to the implicit predictions of most simple biophysical models (3, 24, 25). This may be due to spatial variations in actin filament length and crosslinking density, filament orientation (25), and ratio between numbers of attached and unattached filaments (27), all of which are predicted to affect the magnitude of the net actin force.

Integrating all net normal pressures due to actin over the entire vesicle surface, we find that the component of actin-dependent force that can push the vesicle forward (parallel to the direction of motion) is smaller than the inward compression force (orthogonal to the direction of motion) by 13-fold. That is, most of the force generated by the actin tail is used to compress the vesicle, whereas $<10\%$ of the available force is used to push it.

**Estimated Magnitude of Forces Generated by the Actin Comet Tail.** Although we are able to use the observed vesicle shape to calculate the relative spatial distributions of the pressure components $P_\gamma$ and $P_n$ (Fig. 5 *B–D*), the magnitude of these pressures can be calculated only by knowing the magnitude of the membrane tension $\gamma$. In our experimental system, we cannot directly measure $\gamma$, but we can set limits on its range by considering the material properties of the artificial phospholipid vesicles (see *Supporting Text* and Movie 5, which is published as supporting information on the PNAS web site). Using the estimated lower- and upper-limit values of $\gamma = 0.01-0.1$ mN/m, we can calculate a range of magnitudes of the pressures due to actin at every point on the vesicle surface, because the amount of total integrated actin pressure required to maintain the observed teardrop shapes is linearly proportional to the value of $\gamma$. Integrating the calculated normal actin pressure over the surface of the canonical vesicle shown in Fig. 5*A*, we determined that the minimum amount of net force generated by actin comet tails necessary to maintain this shape is $\approx 0.4-4$ nN. As described above, $<10\%$ of this net force (0.03–0.3 nN) is supplied along the direction of motion; most of the force is orthogonal to the direction of motion and contributes to vesicle distortion.

Our confidence in the force estimate is compromised by two issues. First, proteins in the extract may associate with the surface of the artificial vesicles to change the effective membrane tension in unpredictable ways; and second, the membrane tension for motile vesicles associated with actin comet tails may change over time as the vesicles are increasingly distorted and volume is squeezed out. For these reasons, the upper force limit of 4 nN must be considered provisional. Forces in the nanonewton range are consistent with previous theoretical and experimental analyses (refs. 26, 29, and 44; see *Supporting Text*).

## Discussion

The most important conclusion of this work is that most of the force generated by actin comet tails is compressive rather than propulsive. Our findings indicate that the component of force orthogonal to the direction of motion is >10-fold greater than the component in the direction of motion. Significant compression forces orthogonal to the direction of motion have been predicted by a mesoscopic biophysical model of comet tail force generation where energy released by actin polymerization is stored as elastic deformation in the comet tail actin gel (23, 26, 29, 30). Models of this class consider the actin in the comet tail as a continuous gel that expands when gel growth is catalyzed on a bacterial or bead surface. Strain accumulating in the gel is relieved by forward motion of the object as inward-directed forces are exerted on the curved surface at the rear of the bead or bacterium. Therefore, for deformable objects such as vesicles, compression forces balancing actin gel expansion forces would be predicted to squeeze the object.

Although qualitatively our observations are consistent with this prediction, the model predicts that the largest compressive forces would be positioned at the rear of the cargo (26). In contrast, our results indicate that the net actin polymerization force exerted orthogonal to the direction of motion is greatest on the vesicle sides and minimal at the vesicle rear. In fact, we find that the net forces in the rear of the vesicle are oriented opposite the direction of motion, suggesting a spatial partitioning of pushing and retarding forces, a finding not predicted by any biophysical models to date.

Furthermore, the strain accumulation model predicts that strain must accumulate in the actin gel before forward motion of the cargo (26). In our vesicle system, this would correspond to a negative correlation between vesicle deformation and vesicle speed. The lack of significant correlation between these parameters suggests that temporal partitioning of pushing and retarding forces is not a predominant mechanism for force transduction in this system. These results may be in part explained by the fact that, although the net ratio of pushing to retarding forces may be spatially regulated, the release of retarding attachments at the rear of the vesicle is not synchronized for the entire population of attached filaments. Different actin filaments interacting with the cargo surface may be attached or growing for different amounts of time (27). If the polymerization and binding of each filament are asynchronous and independent of neighboring filaments, their effects would average and result in a continuous strain accumulation and release of friction, instead of a catastrophic release of the vesicle followed by bursts in forward movement as had been previously predicted (26).

Quantitative predictions of the model based on elastic properties of actin comet tails estimate total polymerization forces in the nanonewton range (29, 30), consistent with our estimates of the total net actin-dependent force between 0.4 and 4 nN. We have found that most of this force (93%) is exerted orthogonal to the direction of motion. Vesicles of the size we considered in this study require only 100-fN force to overcome hydrodynamic drag, yet most of the actin polymerization force is exerted orthogonal to the direction of motion, resulting overall in an astonishing inefficiency of the transduction of the chemical energy liberated by actin polymerization into productive forward motion. Other forms of biological movement are also energetically inefficient; for example, the classic flagellar rotor that propels many bacteria through liquid media translates $<1\%$ of the energy required to turn the rotor into forward motion (44). In the actin comet tail, the excess mechanical energy used in compressing the cargo may contribute to the stability and persistence of motion. Intracellular *L. monocytogenes*, for example, readily push their way through dense thickets of organelles. Their actin-dependent motion cannot be slowed by the action of optical tweezers (26) and is slowed only 20-fold with a 500-fold change in the viscoelastic properties of the cytoplasmic extract (45). Slight repartitioning of the powerful mechanical forces at the surface among compression, friction, and propulsion may be sufficient to render this type of actin-based motility very robust to large environmental perturbations. Our results confirm some theoretical predictions of the "tethered ratchet" model (27), where coexisting populations of actin filaments may be exerting different types of forces depending on whether they are bound or under compression. The observation that the net pushing and

retarding forces spatially partition on the sides and rear of the vesicle extends the predictions of this model. See *Supporting Text* for a discussion of possible molecular mechanisms for force partitioning on vesicle surfaces.

In summary, our results directly demonstrate that forces generated by actin comet tails are largely compressive rather than simply propulsive. We show that different types of net actin forces, pushing and retarding, operate on the vesicle surface in a spatially defined manner. Our data rule out a temporally coordinated mechanism of strain accumulation followed by sudden release, contrary to the predictions of mathematical models based on actin gel expansion.

**Note Added in Proof.** Upadhyaya *et al*. (46) have recently reported similar findings.

We thank Matthew Footer for assistance in characterization of the *Xenopus* egg cytoplasmic extract and Tim Stearns and Peter Jackson for providing frogs. We are grateful to members of the Theriot lab for stimulating discussions and to Randy Hampton, Dan Herschlag, Dale Kaiser, James Nelson, Susanne Rafelski, Fred Soo, and Jim Spudich for comments on the manuscript. We also thank Karine Gibbs for assistance with construction of the web site for supporting information. This work was supported by a Fellowship in Science and Engineering from the David and Lucile Packard Foundation (to J.A.T.).

1. Woehlke, G. & Schliwa, M. (2000) *Nat. Rev. Mol. Cell Biol.* **1,** 50–58.
2. Vale, R. D. & Milligan, R. A. (2000) *Science* **288,** 88–95.
3. Hill, T. L. & Kirschner, M. W. (1982) *Int. Rev. Cytol.* **78,** 1–125.
4. Theriot, J. A. (2000) *Traffic* **1,** 19–28.
5. Pantaloni, D., Le Clainche, C. & Carlier, M. F. (2001) *Science* **292,** 1502–1506.
6. Abraham, V. C., Krishnamurthi, V., Taylor, D. L. & Lanni, F. (1999) *Biophys. J.* **77,** 1721–1732.
7. Tilney, L. G. & Portnoy, D. A. (1989) *J. Cell Biol.* **109,** 1597–608.
8. Theriot, J. A., Mitchison, T. J., Tilney, L. G. & Portnoy, D. A. (1992) *Nature* **357,** 257–260.
9. Frischknecht, F. & Way, M. (2001) *Trends Cell Biol.* **11,** 30–38.
10. Ma, L., Rohatgi, R. & Kirschner, M. W. (1998) *Proc. Natl. Acad. Sci. USA* **95,** 15362–15327.
11. Merrifield, C. J., Moss, S. E., Ballestrem, C., Imhof, B. A., Giese, G., Wunderlich, I. & Almers, W. (1999) *Nat. Cell Biol.* **1,** 72–74.
12. Taunton, J., Rowning, B. A., Coughlin, M. L., Wu, M., Moon, R. T., Mitchison, T. J. & Larabell, C. A. (2000) *J. Cell Biol.* **148,** 519–530.
13. Tilney, L. G. & Inoue, S. (1982) *J. Cell Biol.* **93,** 820–827.
14. Cameron, L. A., Svitkina, T. M., Vignjevic, D., Theriot, J. A. & Borisy, G. G. (2001) *Curr. Biol.* **11,** 130–135.
15. Mullins, R. D., Heuser, J. A. & Pollard, T. D. (1998) *Proc. Natl. Acad. Sci. USA* **95,** 6181–6186.
16. Kocks, C., Gouin, E., Tabouret, M., Berche, P., Ohayon, H. & Cossart, P. (1992) *Cell* **68,** 521–531.
17. Welch, M. D., Iwamatsu, A. & Mitchison, T. J. (1997) *Nature* **385,** 265–269.
18. Welch, M. D., Rosenblatt, J., Skoble, J., Portnoy, D. A. & Mitchison, T. J. (1998) *Science* **281,** 105–108.
19. Rohatgi, R., Nollau, P., Ho, H. Y., Kirschner, M. W. & Mayer, B. J. (2001) *J. Biol. Chem.* **276,** 26448–26452.
20. Theriot, J. A., Rosenblatt, J., Portnoy, D., Goldschmidt-Clermont, P. J. & Mitichison, T. J. (1994) *Cell* **76,** 505–517.
21. Cameron, L. A., Footer, M. J., van Oudenaarden, A. & Theriot, J. A. (1999) *Proc. Natl. Acad. Sci. USA* **96,** 4908–4913.
22. Loisel, T. P., Boujemaa, R., Pantaloni, D. & Carlier, M. F. (1999) *Nature* **401,** 613–616.
23. Bernheim-Groswasser, A., Wiesner, S., Golsteyn, R. M., Carlier, M. F. & Sykes, C. (2002) *Nature* **417,** 308–311.
24. Peskin, C. S., Odell, G. M. & Oster, G. F. (1993) *Biophys. J.* **65,** 316–324.
25. Mogilner, A. & Oster, G. (1996) *Biophys. J.* **71,** 3030–3045.
26. Gerbal, F., Chaikin, P., Rabin, Y. & Prost, J. (2000) *Biophys. J.* **79,** 2259–2275.
27. Mogilner, A. & Oster, G. (2003) *Biophys. J.* **84,** 1591–605.
28. Dickinson, R. B. & Purich, D. L. (2002) *Biophys. J.* **82,** 605–617.
29. Gerbal, F., Laurent, V., Ott, A., Carlier, M. F., Chaikin, P. & Prost, J. (2000) *Eur. Biophys. J.* **29,** 134–140.
30. Noireaux, V., Golsteyn, R. M., Friederich, E., Prost, J., Antony, C., Louvard, D. & Sykes, C. (2000) *Biophys. J.* **78,** 1643–1654.
31. Kuo, S. C. & McGrath, J. L. (2000) *Nature* **407,** 1026–1029.
32. Murray. (1991) *Methods Cell Biol.* **36,** 581–605.
33. Pistor, S., Chakraborty, T., Walter, U. & Wehland, J. (1995) *Curr. Biol.* **5,** 517–525.
34. Chakraborty, T., Ebel, F., Domann, E., Niebuhr, K., Gerstel, B., Pistor, S., Temm-Grove, C. J., Jockusch, B. M., Reinhard, M., Walter, U., *et al*. (1995) *EMBO J.* **14,** 1314–1321.
35. Reinhard, M., Halbrugge, M., Scheer, U., Wiegand, C., Jockusch, B. M. & Walter, U. (1992) *EMBO J.* **11,** 2063–2070.
36. Linseisen, F. M., Hetzer, M., Brumm, T. & Bayerl, T. M. (1997) *Biophys. J.* **72,** 1659–1667.
37. Lipowsky, R. & Sackmann, E. (1995) *Structure and Dynamics of Membranes* (Elsevier, Amsterdam).
38. Adamson, A. W. (1990) *Physical Chemistry of Surfaces* (Wiley, New York).
39. Needham, D. & Nunn, R. S. (1990) *Biophys. J.* **58,** 997–1009.
40. Evans, E. & Rawicz, W. (1990) *Phys. Rev. Lett*. **64,** 2094–2097.
41. Rawicz, W., Olbrich, K. C., McIntosh, T., Needham, D. & Evans, E. (2000) *Biophys. J.* **79,** 328–339.
42. Pencer, J., White, G. F. & Hallet, F. R. (2001) *Biophys. J.* **81,** 2716–2728.
43. Berg, H. C. (1993) *Random Walks in Biology* (Princeton Univ. Press, Princeton).
44. Purcell, E. M. (1977) *Am. J. Physiol.* **45,** 3–11.
45. McGrath, J. L., Eungdamrong, N. J., Fisher, C. I., Peng, F., Mahadevan, L., Mitchison, T. J. & Kuo, S. C. (2003) *Curr. Biol.* **13,** 329–332.
46. Upadhyaya, A., Chabot, J. R., Andreeva, A., Samadani, A. & van Oudenaarden, A. (2003) **100,** 4521–4526.